

# AN ANALYSIS OF COMPETING TOUGHENING MECHANISMS IN LAYERED AND PARTICULATE SOLIDS

Giovanni Noselli<sup>\*</sup>, Vikram S. Deshpande and Norman A. Fleck

*Cambridge University Engineering Department, Trumpington Street, Cambridge, CB2 1PZ, UK*

26 February 2013

## Abstract

The potency of various toughening mechanisms is explored for layered solids and particulate solids, containing one or more semi-infinite cracks. First, the enhancement in toughness due to a parallel array of cracks in an elastic solid is explored and the stability of co-operative cracking is quantified. Second, toughening by crack kinking is analysed for a layered solid containing a pre-existing crack. The asymptotic problem of continued, self-similar crack advance versus 90° symmetric kinking is considered. The two competing crack paths involve rupture of cohesive zones, and each crack is endowed with a uniform strength and a critical displacement (at which the traction drops to zero). Third, the evolution of the crack path (and associated crack growth resistance curve) is determined for a regular array of elastic, hexagonal grains bonded together by cohesive zones of finite strength and finite work of separation. Regardless of the initial configuration of a semi-infinite parent crack, with varying degrees of initial crack tip branching, we find that a single dominant crack ensues. The study concludes with the analysis of a mode I crack in a multi-layer stack of elastic and elastic-plastic solids. Plastic dissipation in the ductile layers conveys macroscopic toughening but the degree of toughening is sensitive to the relative height of the layers. The study demonstrates that multiple cracking is a difficult mode to activate under quasi-static conditions and the kinking mechanism, when activated, is potent in enhancing the toughness of a solid.

*Keywords:* toughening mechanisms, multi-layered composites, particulate solids

---

<sup>\*</sup> Telephone: +441223748525; Fax: +441223332662; E-mail: giovanni.noselli@eng.cam.ac.uk

## 1. Introduction

Layered and particulate solids are commonly employed as engineering materials, with applications ranging from lightweight structural parts to high strength coatings. Commonly, high strength composites are brittle, and there is a need to improve their macroscopic toughness by suitable tailoring of topology and interfacial properties. A number of toughening strategies are available, and a major thrust of the current paper is to compare the potency of toughening for some of these strategies. We consider 3 toughening mechanisms in turn: (i) toughening by crack multiplication, (ii) crack kinking, and (iii) toughening by plastic dissipation.

### 1.1. Toughening by crack multiplication

Monolithic ceramics can contain a zone of crack-tip shielding by micro-cracking, see Fig. 1a. This mechanism gives rise to a small elevation in macroscopic toughness, as discussed by Kreher and Pompe (1981), Evans and Faber (1984), Rose (1986), Hutchinson (1987) and Shum and Hutchinson (1990). The effect is modest as the main crack tends to follow the most brittle path. For this mechanism to operate it is essential that the micro-cracks arrest at grain boundaries or particle interfaces and be highly stable in the arrested state. The micro-cracked zone reduces the crack tip stress intensity factor  $K_{\text{tip}}$  by two mechanisms: (i) the micro-cracked zone is more compliant than that of the remote material, and (ii) the micro-cracks release local residual stresses when they form and this leads to a dilatational strain in the micro-cracked zone. However, the degree of crack tip shielding by the micro-cracked zone is only modest. Hutchinson (1987) has shown that the reduction in  $K_{\text{tip}}$  is between 30% and 40% for heavily micro-cracked zones in ceramic materials, as observed by Rühle *et al.* (1990).

We begin by exploring the macroscopic toughening that arises from a parallel array of cracks. Consider a stack of  $n$  parallel semi-infinite cracks under remote mode I  $K$ -field, see Fig. 1b. The magnitude of the crack tip stress intensity factor, and the mode-mix, will vary from crack to crack. Suppose that the cracks were able to adopt a configuration (in terms of relative spacing and relative crack tip position) such that each crack tip is in a state of mode I and has the same tip value of  $K$ . Then, the cracks could, in-principle, advance in a steady-state configuration and the remote applied energy release rate  $G^\infty$  would be  $n$  times the value  $G_{\text{tip}}$  for each crack tip. But this degree of toughening assumes that it is possible for such an array of cracks to be configurationally stable and to adopt a configuration with an identical mode I  $K$ -field for each crack tip. We shall explore whether this is possible for the simple cases of  $n = 2$  and  $n = 3$ .

### 1.2. Crack kinking

Crack tip kinking gives the possibility of toughness elevation for both layered and particulate composites. The case of a layered solid with a pre-existing crack transverse to several layers is shown in Fig. 1c,d. The presence of weak or brittle interfaces between the layers leads to the possibility of crack tip kinking and thereby to crack deflection along the interface. For elastic-brittle interfaces as shown in Fig. 1c, the macroscopic toughness remains constant or decreases when the crack kinks along the interface, as discussed by He and Hutchinson (1989a). Alternatively, the interface may be elastic-plastic in nature, see Fig. 1d, and crack kinking by the progressive failure of this interface can give rise to macroscopic toughening (Cao and Evans 1991; Chan *et al.* 1993; He *et al.* 1993; He *et al.* 1994; Shaw *et al.* 1996).

Now consider intergranular fracture of a particulate elastic solid, with fracture occurring along the interfaces between grains, see Fig. 1e. Potential sources of toughening are crack branching and the simultaneous advance of multiple, connected cracks. Shabir *et al.* (2011) recently conducted a numerical study on the quasi-static fracture of polycrystalline aggregates. They considered an assembly of elastic, randomly-shaped grains, and the grains were connected by cohesive zones. The progressive failure of a specimen containing a single edge crack was addressed, and their quasi-static simulations revealed the progression of a single dominant crack, with minor deviation in path from the initial plane of cracking. A major issue is whether dynamic crack growth is needed in order to achieve multiple branching: Xu and Needleman (1994) observed such kinking behaviour in their simulations of dynamic intergranular crack growth. In the current paper, an attempt is made to gain more insight into the fracture behaviour of particulate solids by exploring the possibility of multiple crack growth in the quasi-static regime from a multiply-branched pre-crack.

### 1.3. Toughening by plastic dissipation

It is generally accepted that plastic dissipation in the vicinity of a crack tip in a ductile solid causes a multiplicative enhancement in macroscopic toughness. This has been demonstrated by Tvergaard and Hutchinson (1992): they calculated the crack growth resistance curve (the so-called R-curve) for a mode I crack in an elastic-plastic solid, with crack advance modelled by a cohesive zone of finite strength and of finite fracture energy. They found that the macroscopic toughness increases with crack advance, until a steady-state is achieved. The steady-state toughness  $G_{ss}^{\infty}$  scales linearly with the cohesive zone energy (as demanded on dimensional grounds), but the degree of toughening increases dramatically with an increase in the ratio of cohesive zone strength to yield strength of the solid.

A closely related problem has been addressed by Suo *et al.* (1993) and by Tvergaard (1997). They replaced the cohesive zone by an elastic strip of mode I toughness  $G_0$  and of finite height  $h$ , see Fig. 1f. Again, an R-curve is predicted, with the level of macroscopic toughening sensitive to the value of  $h$ . We shall extend this approach to the case of a parallel stack of alternating elastic and elastic-plastic layers, with a mode I crack lying on the mid-plane of one elastic strip. Thereby, the degree of toughening within constrained elastic-plastic layers is assessed for a layered composite.

#### 1.4. *Toughening in Nature: the role of structural hierarchy*

Polymer-ceramic composites are ubiquitous in Nature, such as in shell, bone and horn (Currey 1977; Lin and Meyers 2005; Bertoldi *et al.* 2008). Despite the relatively poor mechanical properties of their constituents<sup>1</sup>, these structural biomaterials exhibit a remarkable level of macroscopic toughness and possible reasons for this have been suggested. Several toughening mechanisms have been identified, such as crack bridging, crack blunting, crack tip shielding by the nucleation of micro-voids, and crack deflection along visco-plastic interfaces (Jackson *et al.* 1988; Jackson *et al.* 1990; Wang *et al.* 2001; Gao *et al.* 2003; Espinosa *et al.* 2011; Shao *et al.* 2012). Remarkably, these natural composites are organized in hierarchical microstructures; for example, 3 to 7 levels of structural hierarchy exist in shell and bone, respectively. The precise evolutionary reasons for this remain unclear. One attractive view, as advanced by Gao *et al.* (2006) and Zhang *et al.* (2011), is that structural hierarchy conveys damage tolerance.

#### 1.5. *Overall scope of the study*

The scope of the present study is as follows. In section 2, the enhancement in toughness due to a parallel array of cracks in an elastic solid is explored and the stability of co-operative cracking is quantified. In section 3, toughening by crack kinking is analysed for a layered solid containing a pre-existing transverse crack. The competition between continued crack advance and 90° symmetric kinking is also considered. The two competing crack paths contain cohesive zones, and each cohesive zone is endowed with a strength and toughness. The sensitivity of macroscopic toughness to the relative properties of the two cohesive zones is determined. Further analysis of the significance of crack path upon macroscopic toughness is carried out for intergranular crack advance for a regular array of elastic, hexagonal grains bonded together by cohesive zones of finite strength and fracture

---

<sup>1</sup> Nacre, mother of pearl, is a typical example of a natural structural composite, composed by brittle platelets of aragonite (95 vol%) and thin layers of biopolymers (5 vol%), organized in a brick-and-mortar microstructure.

energy. In section 4, the role of plastic dissipation in controlling toughness of multi-layers is determined: the crack growth resistance curve is predicted for alternating layers of elastic and elastic-plastic solids.

## 2. Toughening of an elastic-brittle solid by multiple cracking

We begin by exploring the possibility of macroscopic toughening for an array of 2 or 3 parallel cracks under remote mode I loading. If these cracks grow simultaneously then macroscopic toughening will exist, but are they configurationally stable? To address this two geometries are analysed: an infinite, elastic-isotropic solid contains either 2 or 3 parallel, semi-infinite cracks, and is subjected to a remote mode I  $K$ -field, see Fig. 2. To address the issue of configurational stability, the crack tips are given a relative off-set, as parameterised by an angle  $\alpha$ . The challenge is to determine the  $K$ -field at each crack tip as a function of  $\alpha$ .

### 2.1. Finite element analysis

Plane strain finite element analyses have been performed in order to extract the crack tip  $K$  as a function of the remote mode I  $K^\infty$ , with the commercial software ABAQUS Standard 6.10-1. Consider an isotropic elastic solid of Young's modulus  $E$  and Poisson's ratio  $\nu$ . A remote mode I  $K$ -field is applied by imposing appropriate displacements  $u_i$  on the outer boundary of the mesh. With  $x_i$  taken as Cartesian co-ordinates centred on the average position of the crack tips, and with the associated polar co-ordinates  $(r, \theta)$ , the displacement field imposed on the outer periphery of the mesh is

$$\begin{cases} u_1 = \frac{K^\infty}{2\mu} \sqrt{\frac{r}{2\pi}} \cos \frac{\theta}{2} (\kappa - \cos \theta) \\ u_2 = \frac{K^\infty}{2\mu} \sqrt{\frac{r}{2\pi}} \sin \frac{\theta}{2} (\kappa - \cos \theta) \end{cases} \quad (1)$$

where  $\mu = E/[2(1+\nu)]$  is the shear modulus, and  $\kappa$  equals  $3-4\nu$  for a state of plane strain. Throughout this study we assume  $\nu = 0.3$ . The finite element meshes are highly refined in the region near the crack tips<sup>2</sup> and comprise CPE4 (plane strain, four-nodes bilinear) elements; converged results were obtained by taking the outer dimension of the mesh to be 250 times the crack spacing. For both geometries the crack tip mode I and mode II stress intensity factors ( $K_I$  and  $K_{II}$ , respectively) are computed by means of the domain-integral method as

---

<sup>2</sup> The dimension of the square finite elements near the crack tips has been fixed to 1/20 the vertical distance between the semi-infinite cracks.

implemented in ABAQUS. Note that the stress intensity factors for tips  $A$  and  $B$  are different, and their relative magnitude gives the requisite information on their configurational stability.

## 2.2. Results

We assume that the direction of crack advance for tips  $A$  and  $B$  of Fig.2 is dictated by the local angle  $\phi = \arctan(K_{II} / K_I)$  for each crack. If  $\phi = 0$ , the crack advances in a self-similar manner, if  $\phi > 0$  the crack tip kinks downwards and if  $\phi < 0$  the crack tip kinks upwards. Whether crack growth occurs or not at each crack tip is also dictated by the energy release rate  $G = (1 - \nu^2)(K_I^2 + K_{II}^2) / E$  in relation to the material toughness  $G_{IC}$ : kinking will occur when  $G$  attains the value  $G = G_{IC} f(\phi)$ , where the function  $f(\phi)$  has been given by Lo (1978) and He and Hutchinson (1989b).

For present purposes it suffices to consider the relative value of  $G$  and  $\phi$  at each crack tip  $A$  and  $B$ , and to normalize the crack tip values for  $G$  by the remote energy release rate  $G^\infty = (1 - \nu^2)(K^\infty)^2 / E$ . Energy release rates are reported in dimensionless form  $G / G^\infty$  in Fig. 3a and in Fig. 4a as a function of  $\alpha$ , for the two- and three-crack geometry, respectively.

Consider first the results for a pair of cracks, of geometry as given in Fig. 2a. When  $\alpha$  is between zero and  $\pi / 2$  (such that crack tip  $A$  is behind tip  $B$ ), we find that the value of  $G$  for tip  $A$  is less than that for tip  $B$ , see Fig. 3a. Consequently, tip  $B$  will advance in preference to tip  $A$ , destabilizing the configuration such that  $\alpha$  reduces further. The phase angle  $\phi$  for tip  $B$  is small and negative implying that the tip  $B$  will veer upwards away from the neighbouring crack  $A$ <sup>3</sup>. In contrast, the geometries  $\pi / 2 < \alpha < \pi$  have the feature that tip  $A$  will kink before tip  $B$  and will kink downwards away from tip  $B$ . Again, the crack tips diverge in path, and in an unstable manner such that the longer crack grows in preference to the shorter crack. The exception is for  $\alpha = \pi / 2$ . Then, the two cracks possess the same value of  $G$ , and  $\phi$  equals 0.3 for tip  $A$  and  $\phi$  equals -0.3 for tip  $B$ , see Fig. 3b: the two cracks kink away from each other. To complete the picture, consider a slight perturbation in crack length such that  $\alpha$  slightly exceeds  $\pi / 2$ . Then the crack tip  $A$  is slightly ahead of tip  $B$ . It will advance in preference to tip  $B$  due to its higher value of  $G$ , and it will diverge (kink) away from tip  $B$ . We conclude that there is a strong tendency for

---

<sup>3</sup> Recall that  $\phi < 0$  implies upwards kinking, whereas  $\phi > 0$  will give downwards kinking, as explained by Lo (1987) for example.

crack growth to shut down for the lagging crack whereas the leading crack will kink away from its passive neighbour.

A similar picture emerges from the case of 3 cracks (Fig. 2b); see computational results in Fig. 4. When  $\alpha < \pi/2$ , crack tip  $A$  lags that of  $B$  and has a much reduced value of  $G$  (Fig. 4a). Consequently, the tips  $B$  will advance and will kink outwards and away from the mid-plane of crack  $A$ . When  $\alpha$  is large (say in the range  $3\pi/4$  to  $\pi$ ), the crack tip  $A$  is far ahead of the tips  $B$  and cracks of type  $B$  have a negligible influence upon it: the crack advances at  $G \approx G^\infty$  and  $\phi \approx 0$ . A cross-over point does exist such that  $G$  for tip  $A$  equals that for tips  $B$  at  $\alpha \approx 1.79$ , corresponding to the case where tip  $A$  is slightly ahead of tip  $B$ . But this configuration is unstable since a slight advance in tip  $A$  will lead to an increased value of  $\alpha$  and thereby to an increased value of  $G$  for tip  $A$  and to a reduced value of  $G$  for tips  $B$ . Again, we conclude that the crack configuration is unstable, with the propensity for crack advance to occur by a single crack, and the shut down of growth by the lagging cracks.

In passing, we note that the values for  $G$  for the 2 cracks of Fig. 2a and for the 3 cracks of Fig. 2b always sum to  $G^\infty$ , as demanded by path independence of the  $J$ -integral (with  $J$  reducing to  $G$  in elastic analysis). Consequently, for geometries where  $G$  values are equal for the crack tips we have  $G/G^\infty = 1/2$  for the pair of cracks (Fig. 2a) and  $G/G^\infty = 1/3$  for the triplet of cracks (Fig. 2b). We emphasise that  $\phi \neq 0$  for each crack tip in the configurations where the  $G$  values are identical: the cracks will kink away from each other.

### 3. Toughening due to interfacial crack kinking

Crack deflection can play a significant role in the failure of particulate, layered and fibre-reinforced composites, recall Fig. 1c-e. Crack kinking can arrest the forward growth of a crack, and act as a potent crack blunting mechanism, particularly when the parent crack kinks into a ductile interface, see Fig. 1d. We shall consider two prototypical problems: (i) crack kinking in a layered solid, as shown in Fig. 5, and (ii) multiple crack branching in a particulate composite, as shown in Fig. 1e. In both cases, the challenge is to obtain the degree of toughening associated with the deviation of crack path from the initial crack plane.

#### 3.1. Crack kinking versus self-similar growth in a layered solid

Crack growth in layered composites or in fibre composites can involve self-similar crack advance ahead of the parent mode I crack or kinking at an angle of  $\phi = \pm\pi/2$ , as shown in Fig. 5. This competition in direction of crack growth has been analysed in the elastic-brittle case by He and Hutchinson (1989a).

Here, we consider ductile interfaces such that the parent crack has a tensile band of strength  $\sigma_y$  and critical opening  $u_p^f$ ; likewise, the crack can kink by the yielding of a shear band of shear strength  $\tau_y$  and failure at a critical shear displacement  $u_k^f$ , see Fig. 5. For simplicity, an ideally plastic response in mode I opening is assumed for the tensile band, and a constant shear resistance exists in the shear band. In the finite element simulations reported below the cohesive zone laws include an elastic loading branch such that the normal traction  $\sigma$  equals  $\sigma_y$  at an opening displacement  $u_p^y = 0.001 u_p^f$ . Similarly, for the shear bands, for computational reasons, the initial response is elastic until the shear traction  $\tau$  attains the yield value  $\tau_y$  at a shear displacement  $u_k^y = 0.001 u_k^f$ . The values of  $(u_p^y, u_k^y)$  are taken to be sufficiently small in relation to  $(u_p^f, u_k^f)$  that the cohesive zones can be treated as rigid, ideally plastic in behaviour. Then, the fracture energy for the normal band equals  $\sigma_y u_p^f$ , whereas the fracture energy for the shear band equals  $\tau_y u_k^f$ .

We are interested in the plane strain, small scale yielding problem such that the parent crack is loaded by a remote mode I stress intensity factor  $K^\infty$ . This is achieved by loading the outer boundary of a square mesh by the asymptotic field (1), as explained in the previous section. There is now the potential for the cohesive zones to shield each other such that the energy release rate at the onset of crack advance  $G_f^\infty$  exceeds both  $\sigma_y u_p^f$  and  $\tau_y u_k^f$ . We explore this behaviour by detailed finite element calculations of the problem as shown in Fig. 5.

Dimensional analysis dictates that

$$\frac{G_f^\infty}{\sigma_y u_p^f} = f_1 \left( \frac{\sigma_y}{\tau_y}, \frac{u_p^f}{u_k^f} \right) \quad (2)$$

and equivalently

$$\frac{G_f^\infty}{\tau_y u_k^f} = f_2 \left( \frac{\sigma_y}{\tau_y}, \frac{u_p^f}{u_k^f} \right) \quad (3)$$

where the functions  $f_1$  and  $f_2$  are to be determined, and the additional independent groups of  $\sigma_y / E$  and Poisson's ratio  $\nu$  are held fixed at 0.003 and 0.3, respectively. We assume that the parent crack advances by kinking when  $\tau_y u_k^f f_2 < \sigma_y u_p^f f_1$  in accordance with relations (2) and (3). Otherwise, self-similar crack advance occurs by failure of the tensile band.

The plane strain finite element calculations were again performed using ABAQUS Standard 6.10-1. The mesh comprises four-nodes bilinear elastic elements (of type CPE4 in ABAQUS notation). Both the tensile cohesive zone (directly ahead of the parent crack) and the two shear cohesive zones (orthogonal to the parent crack) are modelled by COH2D4 elements. The elastic, ideally plastic constitutive laws for the cohesive zones were implemented by means of a user subroutine UMAT. The shear bands are constrained not to open, while the penetration band has no shear traction by symmetry. Numerical experimentation revealed that adequate accuracy is obtained by using at least 20 cohesive elements (of type COH2D4) to model each fracture process zone. The plane strain elements (CPE4) were graded in dimension, and were of side length equal to that of the cohesive elements near the crack tip. Symmetry dictates that only the upper half of the geometry of Fig.5 was analysed. Small scale yielding conditions were ensured by taking the side length of the mesh to exceed 100 times the larger of the two plastic zones at the crack tip.

### 3.1.1. Degree of toughening for crack penetration versus crack kinking

A series of finite element simulations were performed in order to identify the regime of  $(\sigma_y / \tau_y, u_p^f / u_k^f)$  parameters space for which the crack advances by penetration in the tensile band or by kinking along the shear band. The number of required simulations is drastically reduced upon noting that penetration occurs when  $u_p$  attains  $u_p^f$  in the tensile band before  $u_k$  attains  $u_k^f$  in the shear band, and vice versa. Thus, it suffices to increment  $K^\infty$  for a given value of  $\sigma_y / \tau_y$ , and to monitor the maximum opening  $u_p^{\max}$  and the maximum shear displacement  $u_k^{\max}$  as a function of  $K^\infty$ . With increased loading by  $K^\infty$ , a steady-state ratio of  $u_p^{\max} / u_k^{\max}$  is attained and this ratio identifies the value of  $u_p^f / u_k^f$  at which penetration and kinking occur simultaneously.

This procedure is used to identify the boundary between penetration and kinking in Fig.6. Contours of  $G_f^\infty / (\sigma_y u_p^f) \equiv f_1$  and of  $G_f^\infty / (\tau_y u_k^f) \equiv f_2$  are included in the figure, and are also plotted in Fig.7a as a function of  $\sigma_y / \tau_y$ . In order to interpret Fig.7a, we first make use of Fig.6 to identify whether penetration or kinking occurs and then select the appropriate result for  $G_f^\infty$  in Fig.7a.

Likewise, the lengths of the plastic zone for the tensile band  $l_p^f$  and for the shear band  $l_k^f$  are plotted in Fig.7b, and are shown as solid curves for the case of penetration and as dashed curves for kinking. Note that the normalisation of  $(l_p^f, l_k^f)$  is different for the case where penetration or kinking occurs first. The procedure is again

to make use of Fig. 6 in order to determine whether kinking or penetration occurs for any given values of  $\sigma_y / \tau_y$  and  $u_p^f / u_k^f$ . We note from Fig. 6 that the boundary between penetration and kinking is more sensitive to the value of  $\sigma_y / \tau_y$  than to the ratio of  $u_p^f / u_k^f$ . Consequently, the ordinate is plotted as  $(u_p^f - u_k^f) / (u_p^f + u_k^f)$  such that  $u_p^f / u_k^f$  can range from zero to infinity.

To gain additional physical insight, the relative size of the tensile and shear plastic zones is sketched in Fig. 6 for the trajectory  $A \rightarrow B \rightarrow C$  for the choice  $u_p^f = u_k^f$ . There is a marked increase in the size of the shear plastic zone as  $\sigma_y / \tau_y$  increases from zero magnitude at point  $A$  to a large value at point  $C$ . It is clear from both Fig. 6 and from the plot of  $l_p^f \sigma_y / (u_p^f E)$  in Fig. 7b that no shear plastic zone exists for the regime  $\sigma_y / \tau_y < 2.49$ , regardless of the value of  $u_p^f / u_k^f$ . Only penetration is possible within this regime.

The above analysis extends the previous work of Chan *et al.* (1993), and of He *et al.* (1994): these previous studies assumed a shear band of infinite ductility. He *et al.* (1994) employed a linear spring model for the tensile band whereas Chan *et al.* (1993) neglected the presence of a mode I cohesive zone directly ahead of the parent crack. In broad terms, the same trends are observed as in the present study. For example, He *et al.* (1994) showed that the penetration toughness  $G_f^\infty$  increases with diminishing  $\tau_y$ , while Chan *et al.* (1993) revealed that the level of tensile stress ahead of the main crack reduces with diminishing  $\tau_y$ .

### 3.2. Crack path and fracture toughness in particulate solids

The above two sections have separately explored the role of multiple cracking and of crack branching with plasticity in giving rise to macroscopic toughening. We proceed to explore the combined effect of multiple crack branching and crack tip plasticity for a particulate composite.

The challenge is to determine whether a parent mode I crack can give rise to multiple crack branching at its tip, assuming various degrees of *initial* crack branching. The geometry is sketched in Fig. 8; the solid is made up of elastic grains, connected by thin (zero thickness) elastic-plastic interfaces, and contains a semi-infinite parent crack under remote mode I loading. The grains are assumed to be hexagonal in shape with edge length  $d$ , and elastic-isotropic of Young's modulus  $E$  and Poisson's ratio  $\nu$ . As before, small scale yielding and plane strain conditions are assumed, with a remote mode I  $K$ -field imposed, see Fig. 8 and recall (1).

The commercial software ABAQUS 6.10-1 has been employed to perform the computations under quasi-static conditions. Each hexagonal grain is meshed with 96 CPE4R (reduced integration, plane strain, four-nodes bilinear) finite elements, resulting in 4 elements along the side of each hexagon, whereas each interface between the grains has been defined by means of 4 cohesive elements COH2D4. A rectangular domain is employed, of dimension at least 50 times that of the crack tip plastic zone, in order to ensure that small scale yielding conditions prevail. Some initial calculations were performed using the implicit version of ABAQUS but given the large size of the computations, the computational time of those runs was prohibitive. The calculations presented in this study are performed using the explicit solver of ABAQUS in a multi-processor mode (the explicit solver does not require matrix inversion and is thus better suited to parallel execution compared to the implicit solver). Care was taken to ensure that the applied rate of loading was sufficiently slow in the explicit calculations to ensure that material inertial effects are negligible and the results correspond to a quasi-static situation.

### 3.2.1. Specification of the traction-separation law

The interface between neighbouring grains is idealised by a softening cohesive zone law, with cross-coupling between the normal and the tangential components of traction and of displacement. Consider a representative interface with unit normal  $\mathbf{e}_n$  and unit tangential direction  $\mathbf{e}_s$ . Then, the displacement jump  $\mathbf{u}$  across the interface can be expressed in component form  $(u_n, u_s)$  as  $\mathbf{u} = u_n \mathbf{e}_n + u_s \mathbf{e}_s$  and similarly the traction  $\mathbf{t}$  can be written in component form  $(\sigma, \tau)$  as  $\mathbf{t} = \sigma \mathbf{e}_n + \tau \mathbf{e}_s$ .

We assume an elastic-plastic response of the cohesive zone such that the displacement rate  $\dot{\mathbf{u}}$  can be additively decomposed into elastic and plastic components  $\dot{\mathbf{u}}^e$  and  $\dot{\mathbf{u}}^p$ , respectively, giving

$$\dot{\mathbf{u}} = \dot{\mathbf{u}}^e + \dot{\mathbf{u}}^p. \quad (4)$$

The traction rate  $\dot{\mathbf{t}}$  is linear and taken to be co-directional in  $\dot{\mathbf{u}}^e$ , and is related by a scalar spring stiffness  $k$  such that

$$\dot{\mathbf{t}} = k \dot{\mathbf{u}}^e. \quad (5)$$

Plastic collapse occurs when an effective traction

$$t_e \equiv \sqrt{\sigma^2 + \tau^2} \quad (6)$$

attains a yield value  $t_y$ . Upon writing  $\dot{u}_n^p$  and  $\dot{u}_s^p$  as the plastic work conjugates to  $\sigma$  and  $\tau$ , respectively, an effective displacement rate  $\dot{u}_e$  is introduced as

$$\dot{u}_e \equiv \sqrt{(\dot{u}_n^p)^2 + (\dot{u}_s^p)^2}. \quad (7)$$

We proceed in the usual way for a plastic solid: assume normality of plastic flow such that

$$\dot{u}_n^p = \frac{\partial t_e}{\partial \sigma} \frac{\dot{t}_e}{h}$$

and

$$\dot{u}_s^p = \frac{\partial t_e}{\partial \tau} \frac{\dot{t}_e}{h}$$

in terms of a hardening modulus  $h$ . We shall subsequently consider the softening case with  $h$  negative. Upon making use of (6) and (7) we can write  $h$  as

$$h = \frac{dt_e}{du_e}. \quad (9)$$

The incremental constitutive law follows as

$$\dot{\mathbf{t}} = k\dot{\mathbf{u}} - \frac{k^2(\mathbf{t} \cdot \dot{\mathbf{u}})}{t_e^2(k+h)} \mathbf{t} \quad (10)$$

for plastic loading, and

$$\dot{\mathbf{t}} = k\dot{\mathbf{u}} \quad (11)$$

for elastic unloading. The rate of dissipated energy per unit area of interface is

$$\dot{G}_0 = \mathbf{t} \cdot \dot{\mathbf{u}}_p = t_e \dot{u}_e. \quad (12)$$

It remains to specify the relation between  $t_y$  and  $u_e$ . A softening law is adopted here, such that

$$t_y = t_0 + hu_e \quad (13)$$

in terms of an initial strength  $t_0$  and a linear softening parameter  $h$ , of negative magnitude. The plastic work of separation  $G_0$  is obtained by integration of (12) to obtain via (13)

$$G_0 = -\frac{t_0^2}{2h}. \quad (14)$$

The above constitutive law for the interface has been implemented in ABAQUS by means of a user subroutine VUMAT and employing the elastic predictor-plastic corrector algorithm, see Lubliner (1990).

### 3.2.2. Dimensional analysis and results

Two reference quantities are now introduced and will be used for normalisation of the numerical results: a reference stress intensity factor

$$K_0 = \sqrt{\frac{E G_0}{1-\nu^2}}, \quad (15)$$

and a reference material length

$$R_0 = \frac{2}{\pi} \left( \frac{K_0}{t_0} \right)^2, \quad (16)$$

which sets the length scale for the plastic zone size.

The predicted R-curve response,  $K^\infty$  versus the arc length of crack extension  $\Delta a$ , has the following dimensionless form

$$\frac{K^\infty}{K_0} = f_3 \left( \frac{\Delta a}{R_0}, \frac{R_0}{d}, \frac{t_0}{E}, \frac{k d}{E} \right), \quad (17)$$

in terms of an unknown function  $f_3$ . After sufficient crack extension, a steady-state value of stress intensity factor  $K_{SS}^\infty$  is attained. Our primary aim is to explore the dependence of the R-curve upon selected initial configurations of the crack tip, as shown in the inserts of Figs. 9 and 11, for the choice  $t_0/E = 0.003$ ,  $k d/E = 100$ ,  $\nu = 0.3$  and for the two choices  $R_0/d = 1$  and  $R_0/d = 7$ . The case  $R_0/d = 1$  corresponds to the case where the plastic zone is comparable to the particle size, whereas the plastic zone size much exceeds the particle size at  $R_0/d = 7$ . The initial crack tip configuration comprises the following 4 choices: a single crack, a branched crack, a doubly branched crack and a micro-crack of length  $d$  directly ahead of a singly-branched parent crack tip.

The predicted crack paths and associated R-curves are given in Figs. 9 and 10, respectively, for the choice  $R_0/d = 1$ . Likewise, the predicted crack paths and associated R-curves are reported in Figs. 11 and 12 for the choice  $R_0/d = 7$ . Note that the displacement field in Figs. 9 and 11 is magnified by a factor 10, while the red colour refers to traction-free fresh crack surface. The predicted crack trajectories and R-curves are remarkably independent of the magnitude of crack tip toughness and of the initial configuration of the crack tip. For the case (a) of an unbranched initial crack the R-curve begins at  $K^\infty \simeq K_0$  for  $R_0/d = 1$ , and  $K^\infty \simeq 1.25 K_0$  for  $R_0/d = 7$ . Initial branching of the crack leads to a somewhat higher value of  $K^\infty$  at the initiation of crack growth. We note that in all cases a single crack advances, despite the fact that several crack tips may exist in the initial configuration<sup>4</sup>. Further, there is only a minor elevation of crack growth resistance with crack advance. This is

---

<sup>4</sup> This contrasts with dynamic fracture where crack branching is ubiquitous, Lawn (1993).

consistent with the fact that the cohesive zone is softening in nature and thereby promotes plastic localisation of deformation as also observed by Shabir *et al.* (2011).

#### 4. The mode I crack growth resistance of multi-layered, elastic-plastic composites

Multi-layered solids, comprising an elastic brittle phase and a much tougher elastic-plastic phase are increasingly used in engineering application, from the joining of metallic parts by an adhesive layer to electronic devices. Failure within the elastic layer is of general concern, and the question arises: to what degree does the presence of the elastic-plastic layers enhance the macroscopic toughness?

A prototypical plane strain geometry is shown in Fig. 13a: an elastic strip of height  $h$  contains a semi-infinite crack, and is sandwiched between two elastic-perfectly plastic half-planes. This problem has been previously investigated by Suo *et al.* (1993) and Tvergaard (1997). The fracture energy for the central strip is denoted by  $G_0$ , and  $\sigma_y$  is the yield strength of the elastic-plastic phase. Both the elastic strip and the elastic-plastic substrates have a Young's modulus and a Poisson's ratio  $E$  and  $\nu$ , respectively. Displacements are imposed on the outer periphery according to the field (1), so that the magnitude of the external loading is given by the remote stress intensity factor  $K^\infty$ . The onset of crack growth occurs when the remote stress intensity factor  $K^\infty$  attains the value  $K_0 = \sqrt{EG_0 / (1-\nu^2)}$ . Upon increasing  $K^\infty$ , the crack advances through the elastic strip until a steady-state is attained, such that the crack advances at  $K^\infty$  equal to  $K_{ss}^\infty$ . The numerical analyses, carried out by Suo *et al.* (1993) under plane strain and small scale yielding conditions, revealed that the macroscopic steady-state toughness  $K_{ss}^\infty / K_0$  is a maximum as  $h$  tends to zero, see for instance Fig. 5 in Suo *et al.* (1993).

These results are now generalized in order to compute the mode I crack growth resistance of an elastic-plastic, multi-layered composites, consisting of alternating elastic and elastic-perfectly plastic strips of height  $h$  and  $H$ , respectively, see Fig. 13b. Again, the semi-infinite crack is placed along the centre-line of the central elastic layer.

The R-curve of the layered solid,  $K^\infty$  versus  $\Delta a$ , now depends upon a set of four dimensionless parameters,

$$\frac{K^\infty}{K_0} = f_4 \left( \frac{\Delta a}{R_0}, \frac{h}{R_0}, \frac{H}{R_0}, \varepsilon_y \right), \quad (18)$$

where the reference length  $R_0$  is now taken to be the plane strain plastic zone size for  $K^\infty$  equal to  $K_0$ ,

$$R_0 = \frac{1}{3\pi} \left( \frac{K_0}{\sigma_y} \right)^2. \quad (19)$$

#### 4.1. Specification of the finite element model and numerical results

The finite element computations, performed with ABAQUS Standard 6.10-1, required highly refined meshes in the process zone near the crack tip; CPE4 (plane strain, four-nodes bilinear) finite elements have been used and converged results have been obtained taking their dimension equal to  $R_0/30$ . Moreover, at least 5 elements have been employed through the thickness of the elastic and elastic-plastic strips and, to enforce the small scale yielding conditions assumed in the computations, the outer dimension of the meshes exceeds 50 times the maximum extension on the plastic zone at failure. By symmetry considerations about the central horizontal axis, only the upper half of the geometry has been meshed, with zero traction imposed on the crack plane and zero normal displacement on the remaining portion of the symmetry plane ahead of the initial crack tip.

We remark here that the results by Suo *et al.* (1993) have been obtained employing an iterative finite element procedure, as developed by Dean and Hutchinson (1980), in which the steady-state condition of quasi-static crack growth is directly satisfied, whereas, in our analyses, R-curves have been determined explicitly. For this purpose, the strategy of Tvergaard (1997) has been used, based on the evaluation of the  $J$ -integral at the crack tip,  $J_{\text{tip}}$ , with crack growth obtained by successive node-release when the condition  $J_{\text{tip}} = G_0$  is satisfied.

Resistance curves for the multi-layered composite have been computed taking  $\varepsilon_y = 0.003$ ,  $\nu = 0.3$ ,  $h/R_0 = \{0.58, 0.33, 0.18\}$  and  $H/R_0$  ranging from 0 up to 100. Selected results are shown in Fig. 14 as dashed-dotted and dashed curves, for  $H/R_0 = \{0.85, 1.70\}$  respectively, and are compared with the solid curve for  $H/R_0 = \infty$  corresponding to the problem as sketched in Fig. 13a. We conclude that  $H/R_0 = \infty$  provides an upper limit on the R-curve for any height of elastic strip  $h/R_0$ . A simple interpretation is as follows. Most of the elevation in toughness is due to non-proportional loading of the plastically deformed material immediately adjacent to the central elastic strip. Thus a reduction in the magnitude of  $h/R_0$  elevates the toughness. A smaller effect is observed for  $H/R_0$ : there is a small elevation in toughness as  $H/R_0$  is increased from 1.7 to infinity. The relative sensitivity of toughening to  $h/R_0$  and to  $H/R_0$  is further explored in Fig. 15; the figure gives the sensitivity of the steady state toughness  $K_{\text{ss}}^\infty / K_0$  to  $H/R_0$  for selected values of  $h/R_0$ . A sketch of the initial

stationary plastic zone is shown in the insert to the figure for  $h/R_0 = 0.18$ , and for both small and large  $H/R_0$ . Since most of the plastic dissipation takes place in material elements close to the crack tip,  $K_{ss}^\infty / K_0$  increases sharply when  $h/R_0$  is reduced from 0.33 to 0.18 and when  $H/R_0$  is increased from zero to about unity. For any given value of  $h/R_0$ , a threshold for  $H/R_0$  exists above which the fracture toughness of the layered solid is constant: this is set by the condition that the active plastic zone just reaches the outer boundary of the first elastic-plastic layer adjacent to the crack. At the other extreme, as  $H/R_0$  tends to zero, no toughening by plastic dissipation is possible and  $K_{ss}^\infty / K_0$  tends to unity.

## 5. Discussion and concluding remarks

In this study, finite element computations have been performed in order to explore the relative potency of toughening mechanism by crack branching, crack multiplication and by plasticity in layered solids. In most cases, the predicted degree of toughening is only moderate, as it is remarkably difficult to attain a state of crack multiplication when a cohesive zone of finite tip toughness exists at the crack tip: unloading occurs in the wake of a single dominant crack. The study thus suggests that multiple crack branching requires additional physics such as dynamic effects at the crack tip. The competition between crack penetration and crack kinking at an interface is also explored, and it is shown that the direction of crack advance is sensitive to both the relative strength and relative toughness of the cohesive zones associated with penetration or kinking. The kinking mechanism is shown to be able to significantly increase the macroscopic toughness of the solid: it is the most potent of the mechanisms considered here in terms of enhancing toughness.

## Acknowledgements

The authors are grateful to DARPA for their financial support through grant W91CRB-10-1-005 titled “A micro-cellular solids approach to thermo-structural materials with controlled architecture”.

## References

- [1] ABAQUS Theory Manual, version 6.10 (2010) Hibbitt, Karlsson and Sorensen, Inc., Pawtucket, R.I., USA.
- [2] Bertoldi K, Bigoni D and Drugan WJ (2008) Nacre: an orthotropic and bimodular elastic material. *Compos Sci Technol* 68:1363-1375.
- [3] Cao HC and Evans AG (1991) On crack extension in ductile/brittle laminates. *Acta Metall Mater* 39:2997-3005.
- [4] Chan KS, He M-Y and Hutchinson JW (1993) Cracking and stress redistribution in ceramic layered composites. *Mater Sci Eng A* 167:57-64.

- [5] Currey JD (1977) Mechanical properties of mother of pearl in tension. *Proc R Soc Lond B* 196:443-463.
- [6] Dean RH and Hutchinson JW (1980) Quasi-static crack growth in small-scale yielding. In: *Fracture Mechanics. Proceedings of the Twelfth National Symposium of Fracture Mechanics*, ASTM STP 700, American Society for Testing and Materials, pp 383-405.
- [7] Evans AG and Faber KT (1984) Crack-growth resistance of microcracking brittle materials. *J Am Ceram Soc* 67:255-260.
- [8] Espinosa HD, Juster AL, Latourte FJ, Loh OY, Gregoire D and Zavattieri PD (2011) Tablet-level origin of toughening in abalone shells and translation to synthetic composite materials. *Nature Commun* 2:1-9.
- [9] Gao H, Ji B, Jäger IL, Arzt E and Fratzl P (2003) Materials become insensitive to flaws at the nanoscale: lesson from nature. *Proc Natl Acad Sci USA* 100:5597-5600.
- [10] Gao H (2006) Application of fracture mechanics concepts to hierarchical biomechanics of bone and bone-like materials. *Int J Fract* 138:101-137.
- [11] He M-Y and Hutchinson JW (1989a) Crack deflection at an interface between dissimilar elastic materials. *Int J Solid Structures* 25:1053-1067.
- [12] He M-Y and Hutchinson JW (1989b) Kinking of a crack out of an interface. *J Appl Mech* 56:270-278.
- [13] He M-Y, Heredia FE, Wissuchek DJ, Shaw MC and Evans AG (1993) The mechanics of crack growth in layered materials. *Acta Metall Mater* 41:1223-1228.
- [14] He M-Y, Wu B and Suo Z (1994) Notch-sensitivity and shear bands in brittle matrix composites. *Acta Metall Mater* 42:3065-3070.
- [15] Hutchinson JW (1987) Crack tip shielding by micro-cracking in brittle solids. *Acta Metall Mater* 35:1605-1619.
- [16] Jackson AP, Vincent JFV and Turner RM (1988) The mechanical design of nacre. *Proc R Soc Lond B* 234:415-440.
- [17] Jackson AP, Vincent JFV and Turner RM (1990) Comparison of nacre with other ceramic composites. *J Mater Sci* 25:3173-3178.
- [18] Kreher W and Pompe W (1981) Increased fracture toughness of ceramics by energy-dissipative mechanisms. *J Mater Sci* 16:694-706.
- [19] Lawn B (1993) *Fracture of brittle solids*. Cambridge University Press.
- [20] Lin A and Meyers MA (2005) Growth and structure in abalone shell. *Mater Sci Eng A* 390:27-41.
- [21] Lo KK (1978) Analysis of branched cracks. *J Appl Mech* 45:797-802.
- [22] Lubliner J (1990) *Plasticity theory*. Pearson Education.
- [23] Rose LRF (1986) Microcrack interaction with a main crack. *Int J Fract* 31:233-242.
- [24] Rühle M, Evans AG, McMeeking RM, Charalambides PG and Hutchinson JW (1987) Microcrack toughening in alumina/zirconia. *Acta Metall Mater* 35:2701-2710.
- [25] Shabir Z, Van der Giessen E, Duarte CA and Simone A (2011) The role of cohesive properties on intergranular crack propagation in brittle polycrystals. *Modelling Simul Mater Sci Eng* 19:1-21.
- [26] Shao Y, Zhao H-P, Feng X-Q and Gao H (2012) Discontinuous crack-bridging model for fracture toughness analysis of nacre. *J Mech Phys Solids* 60:1400-1419.
- [27] Shaw MC, Clyne TW, Cocks ACF, Fleck NA and Pateras SK (1996) Cracking patterns in metal-ceramic laminates: effects of plasticity. *J Mech Phys Solids* 44:801-821.
- [28] Shum DKM and Hutchinson JW (1990) On toughening by microcracks. *Mech Materials* 9:83-91.
- [29] Suo Z, Shih C and Varias AG (1993) A theory for cleavage cracking in the presence of plastic flow. *Acta Metall Mater* 41:1551-1557.
- [30] Tvergaard V and Hutchinson JW (1992) The relation between crack growth resistance and fracture process parameters in elastic-plastic solids. *J Mech Phys Solids* 40:1377-1397.
- [31] Tvergaard V (1997) Cleavage crack growth resistance due to plastic flow around a near-tip dislocation-free region. *J Mech Phys Solids* 45:1007-1023.

- [32] Wang RZ, Suo Z, Evans AG, Yao N and Aksay IA (2001) Deformation mechanisms in nacre. *J Mater Res* 16:2485-2493.
- [33] Xu X-P and Needleman A (1994) Numerical simulations of fast crack growth in brittle solids. *J Mech Phys Solids* 42:1397-1434.
- [34] Zhang Z, Zhang Y-W and Gao H (2011) On optimal hierarchy of load-bearing biological materials. *Proc R Soc Lond B* 278:519-525.

## List of figures captions

**Fig. 1:** A schematic representation of potential toughening mechanisms: (a) stress-induced micro-cracking in monolithic ceramics; (b) crack multiplication; (c) crack kinking in layered solids along a brittle interface; (d) crack kinking in layered solids along a ductile interface; (e) crack deflection and crack branching in particulate solids; and (f) plastic dissipation in a ductile phase.

**Fig. 2:** An elastic, isotropic solid containing (a) 2 and (b) 3 semi-infinite, parallel cracks. The geometry depicted in (b) is symmetric about the central horizontal axis, whereas that in (a) is not. In both cases, the configuration of the cracks is uniquely defined by the angle  $\alpha$ , and displacements are imposed on the outer periphery of the solid according to the asymptotic mode I  $K$ -field centred on the average position of the crack tips.

**Fig. 3:** (a) The dimensionless energy release rates  $G/G^\infty$  (b) and phase angles  $\phi = \arctan(K_{II}/K_I)$  as a function of  $\alpha$  for the 2 cracks geometry shown in Fig. 2a. Results are reported for both the cracks labeled 'A' and 'B'.

**Fig. 4:** (a) The dimensionless energy release rates  $G/G^\infty$  and (b) phase angles  $\phi = \arctan(K_{II}/K_I)$  as a function of  $\alpha$  for the 3 cracks geometry shown in Fig. 2b. Results are reported for both the central crack labeled 'A' and for the two cracks labeled 'B'.

**Fig. 5:** A layered solid containing a semi-infinite initial crack remotely loaded by means of the mode I asymptotic  $K$ -field. The competition between fracture by forward crack growth and kinking is modeled via the tensile and shear cohesive zones depicted in the diagram.

**Fig. 6:** Map illustrating the regimes of dominance of forward crack growth (penetration) and crack kinking. Contours of the predicted macroscopic toughness are included for selected values of  $G_f^\infty / (\sigma_y u_p^f)$  and  $G_f^\infty / (\tau_y u_k^f)$  along with sketches illustrating the relative sizes of the forward and kinking plastic zones for the 3 cases labelled 'A' through 'C' on the map.

**Fig. 7:** The predicted (a) toughness and (b) lengths of the plastic tensile and shear bands as a function of  $\sigma_y / \tau_y$ . The dashed and solid curves pertain to situations that lie within the kinking and penetration regimes, respectively of the map in Fig. 6.

**Fig. 8:** A cracked particulate solid made up of hexagonal elastic grains of dimension  $d$  and glued together by zero thickness elastic-plastic interfaces. The solid is loaded by applying on its boundary the asymptotic mode I  $K$ -field. The effective traction-separation law for the interfaces is depicted in the inset.

**Fig. 9:** Finite element predictions of the crack paths (shaded in red) for the particulate solid with  $t_0/E = 0.003$ ,  $kd/E = 100$  and  $R_0/d = 1$ . Four initial crack configurations are considered in (a) through (d) as depicted in the insets. The displacement field is magnified by a factor 10 in order to better illustrate the crack paths.

**Fig. 10:** Predictions of the R-curves for the particulate solid with  $t_0/E = 0.003$ ,  $kd/E = 100$  and  $R_0/d = 1$ . Results for four cases corresponding to the initial crack configurations (a) through (d) shown in Fig. 9 are included.

**Fig. 11:** Finite element predictions of the crack paths (shaded in red) for the particulate solid with  $t_0/E = 0.003$ ,  $kd/E = 100$  and  $R_0/d = 7$ . Four initial crack configurations are considered in (a) through (d) as depicted in the insets. The displacement field is magnified by a factor 10 in order to better illustrate the crack paths.

**Fig. 12:** Predictions of the R-curves for the particulate solid with  $t_0/E = 0.003$ ,  $kd/E = 100$  and  $R_0/d = 7$ . Results for four cases corresponding to the initial crack configurations (a) through (d) shown in Fig. 11 are included.

**Fig. 13:** (a) Sketch of the crack in an elastic layer sandwiched between elastic-plastic solids as analyzed by Suo *et al.* (1993) and Tvergaard (1997). (b) Sketch of the cracked multi-layered elastic-plastic composite comprising alternating elastic and elastic-plastic layers of height  $h$  and  $H$ , respectively. The crack lies within an elastic layer as depicted in (b). Both geometries are subjected to a remote mode I  $K$ -field.

**Fig. 14:** Predictions of the R-curves for the multi-layer composite of Fig.13b for the selected values of  $h/R_0$  and  $H/R_0$ . For each value of  $h/R_0$  we have also included the predicted R-curve for the geometry of Fig. 13a: these results are identical to those presented by Suo *et al.* (1993) and Tvergaard (1997).

**Fig. 15:** Predictions of the steady-state macroscopic toughness  $K_{ss}^\infty/K_0$  in the multi-layered composite of Fig.13b as a function of  $H/R_0$  for selected values of  $h/R_0$ . Sketches depicting the plastic zones for large and small values of  $H$  are included in the inset.

List of figures

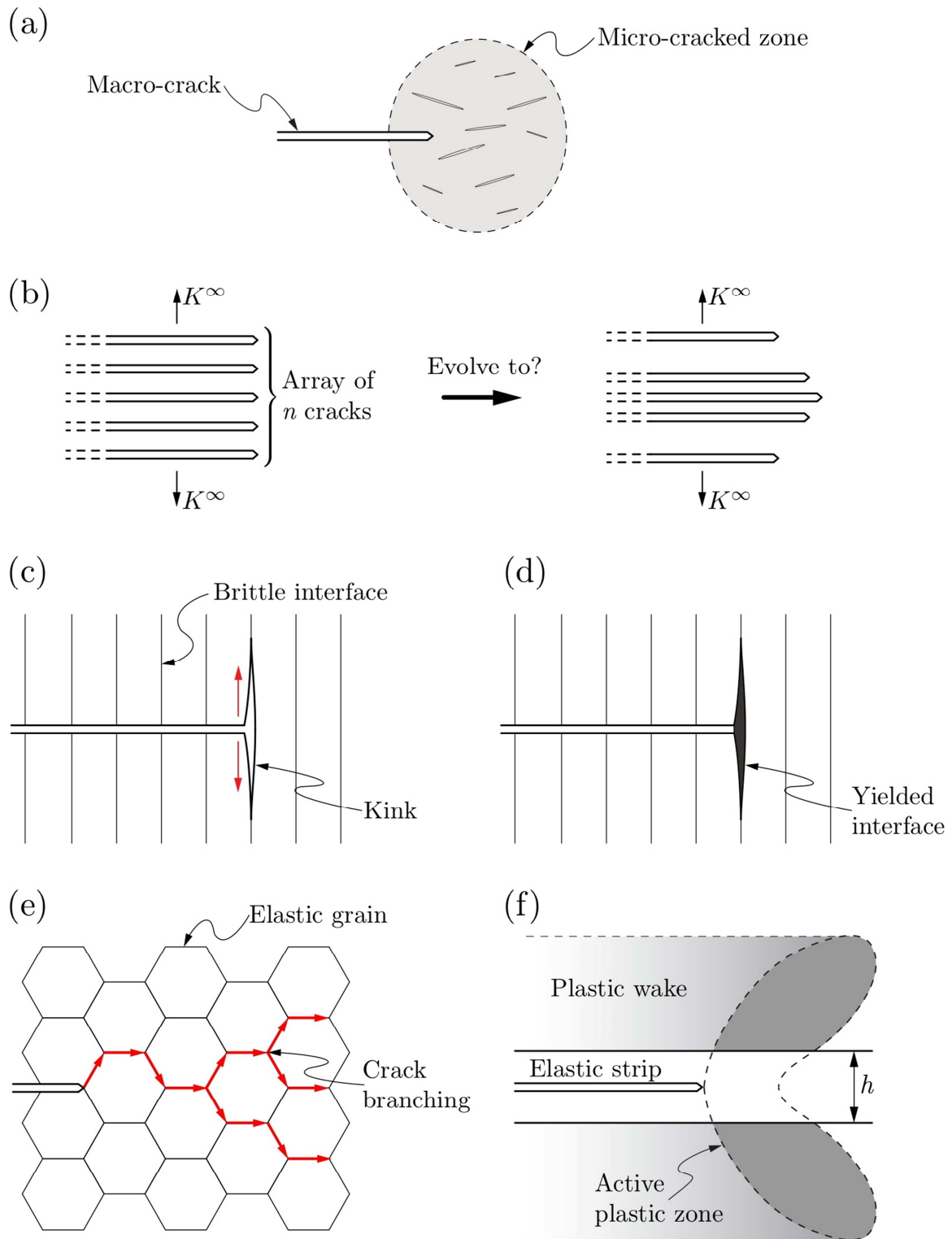


**Fig. 1:** A schematic representation of potential toughening mechanisms: (a) stress-induced micro-cracking in monolithic ceramics; (b) crack multiplication; (c) crack kinking in layered solids along a brittle interface; (d) crack kinking in layered solids along a ductile interface; (e) crack deflection and crack branching in particulate solids; and (f) plastic dissipation in a ductile phase.

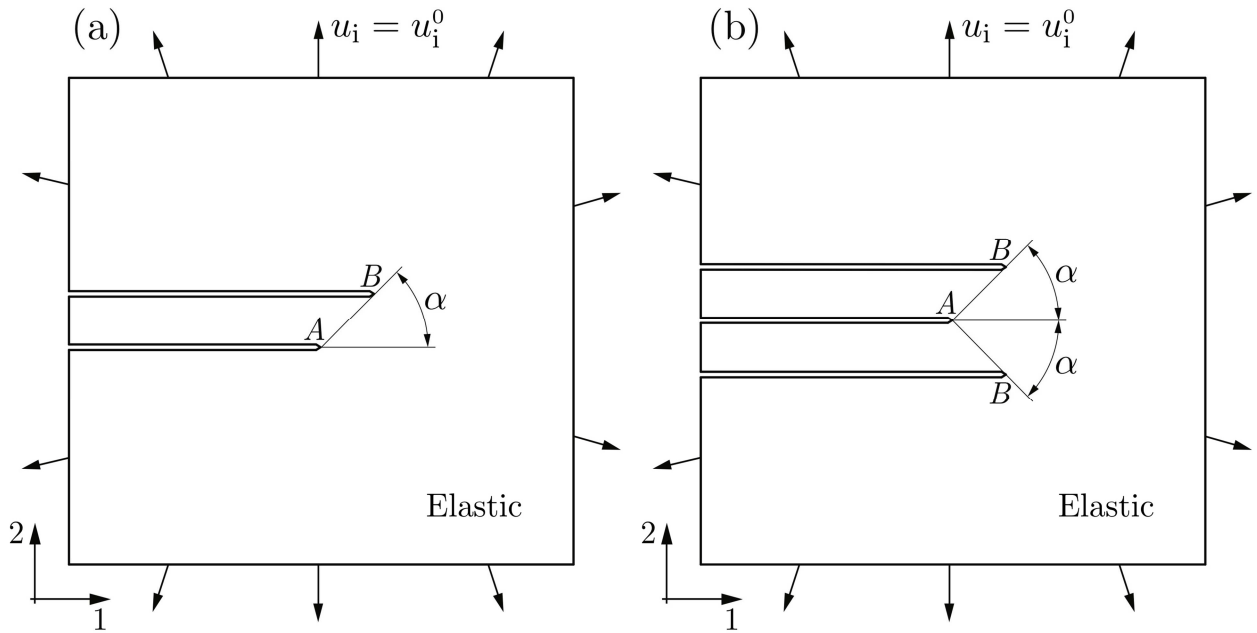


**Fig. 2:** An elastic, isotropic solid containing (a) 2 and (b) 3 semi-infinite, parallel cracks. The geometry depicted in (b) is symmetric about the central horizontal axis, whereas that in (a) is not. In both cases, the configuration of the cracks is uniquely defined by the angle  $\alpha$ , and displacements are imposed on the outer periphery of the solid according to the asymptotic mode I  $K$ -field centred on the average position of the crack tips.

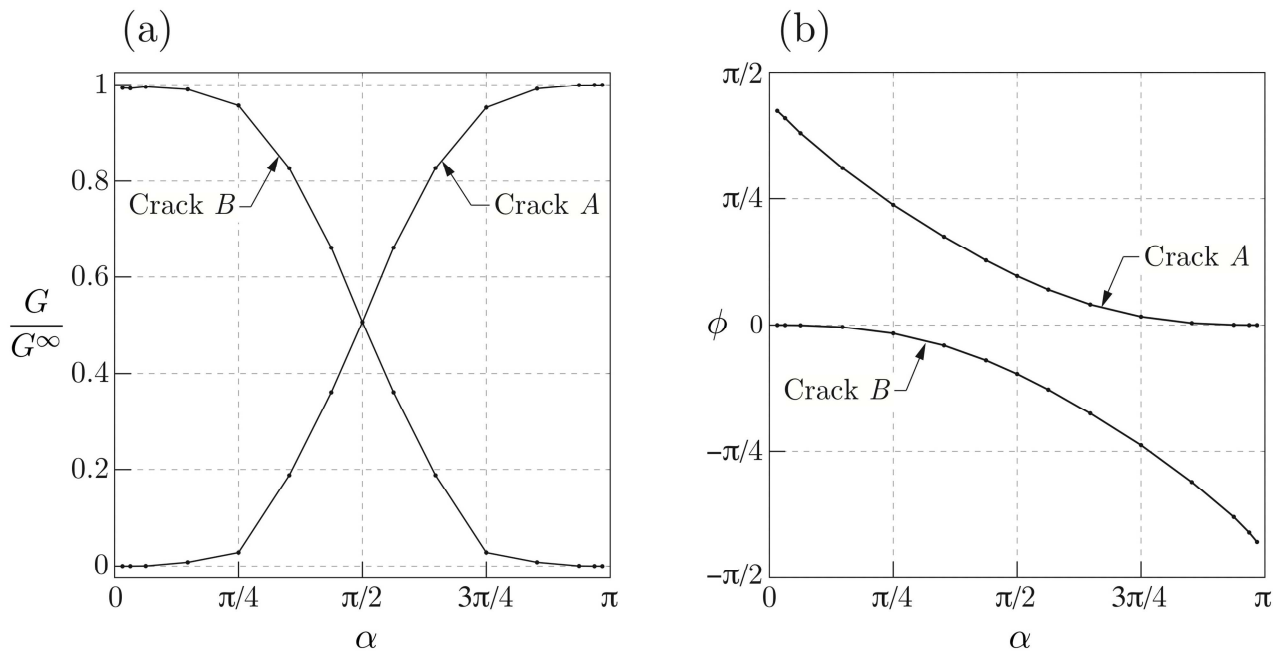


**Fig. 3:** (a) The dimensionless energy release rates  $G/G^\infty$  (b) and phase angles  $\phi = \arctan(K_{II}/K_I)$  as a function of  $\alpha$  for the 2 cracks geometry shown in Fig. 2a. Results are reported for both the cracks labeled 'A' and 'B'.

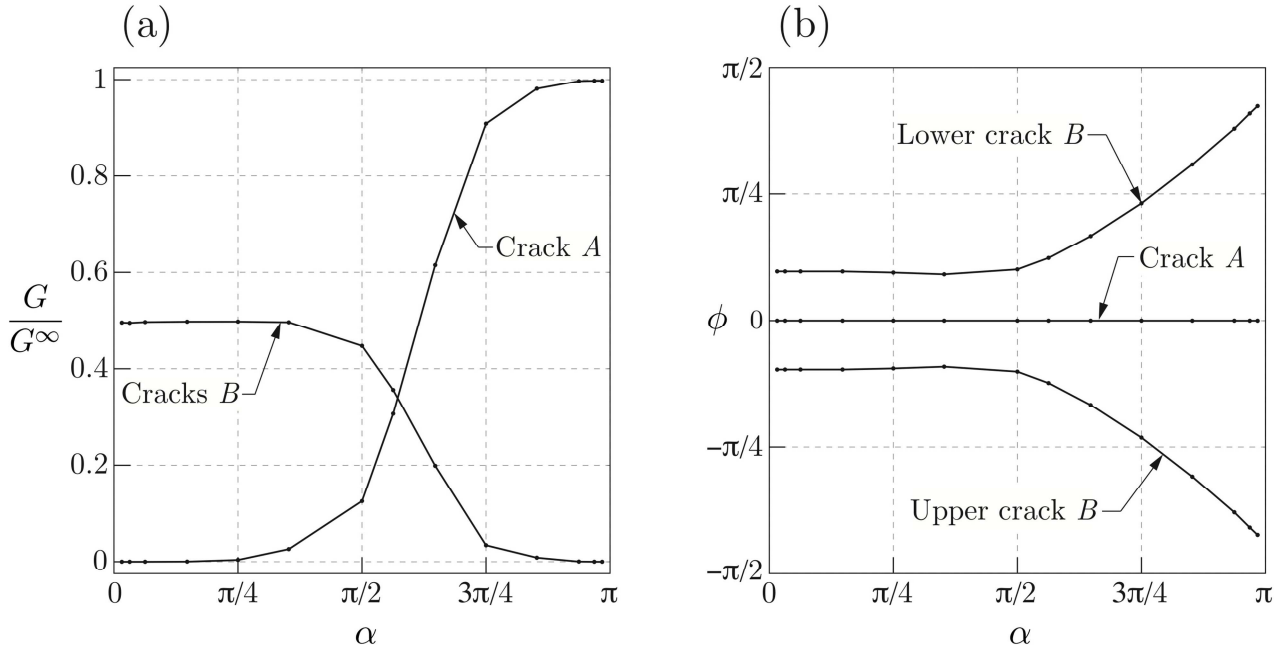


**Fig. 4:** (a) The dimensionless energy release rates  $G/G^\infty$  and (b) phase angles  $\phi = \arctan(K_{II}/K_I)$  as a function of  $\alpha$  for the 3 cracks geometry shown in Fig. 2b. Results are reported for both the central crack labeled 'A' and for the two cracks labeled 'B'.

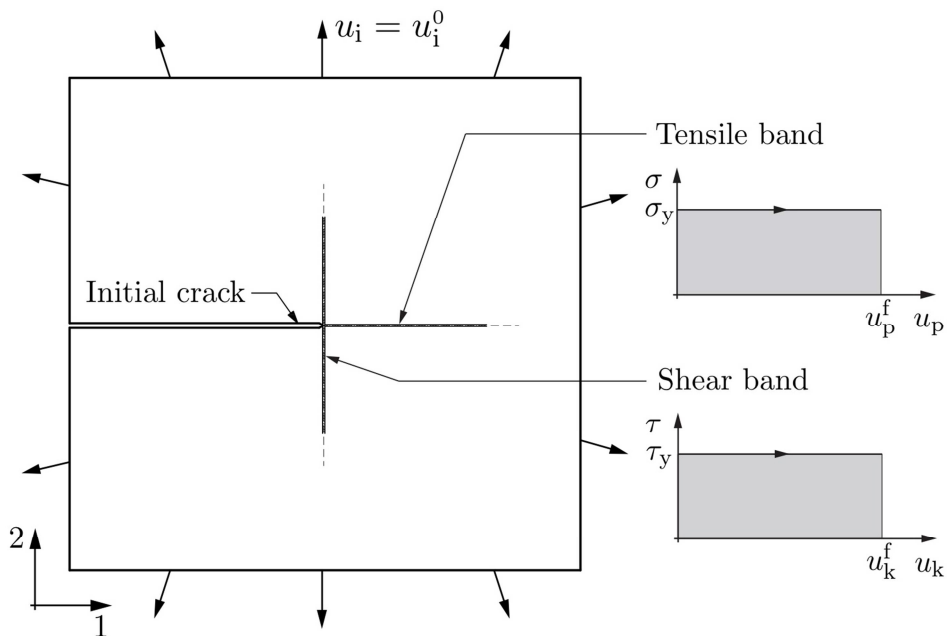


**Fig. 5:** A layered solid containing a semi-infinite initial crack remotely loaded by means of the mode I asymptotic  $K$ -field. The competition between fracture by forward crack growth and kinking is modeled via the tensile and shear cohesive zones depicted in the diagram.

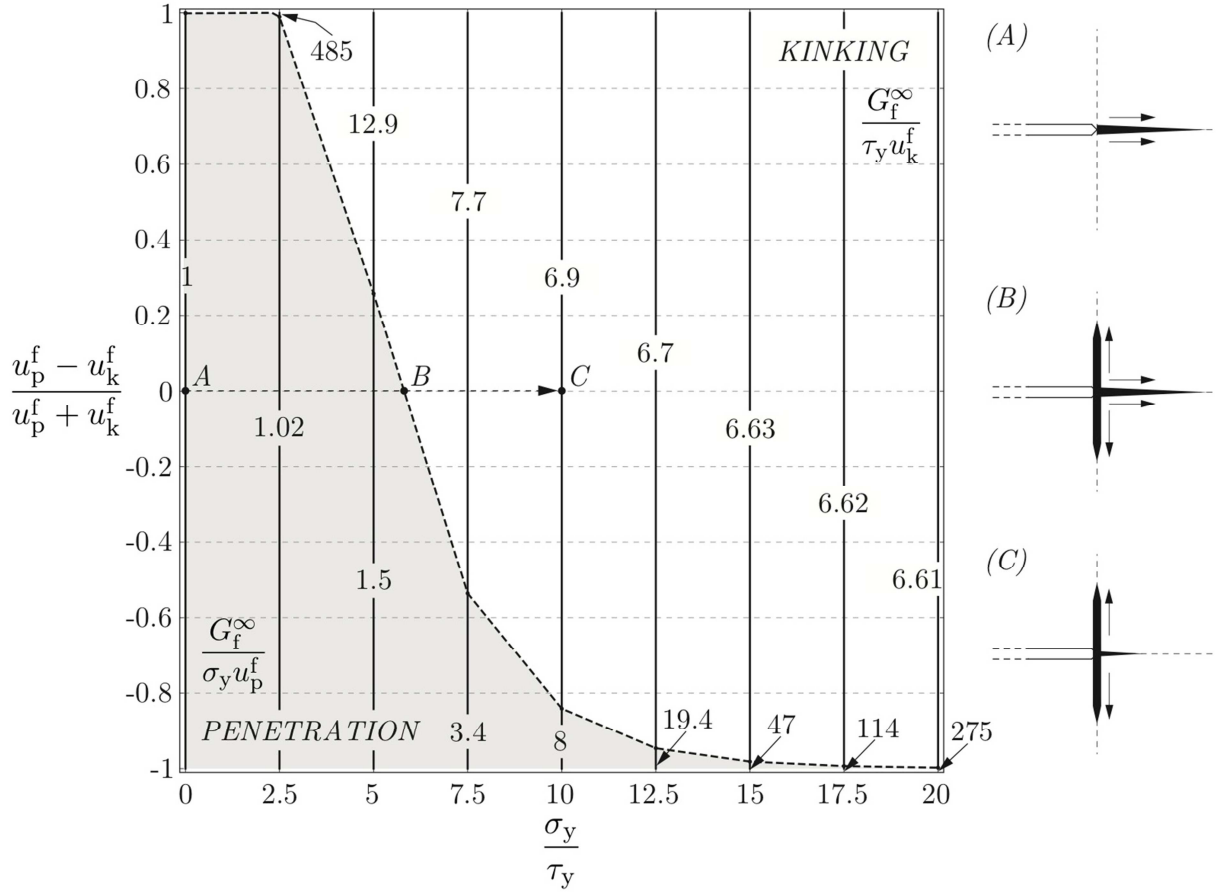


**Fig. 6:** Map illustrating the regimes of dominance of forward crack growth (penetration) and crack kinking. Contours of the predicted macroscopic toughness are included for selected values of  $G_f^\infty / (\sigma_y u_p^f)$  and  $G_f^\infty / (\tau_y u_k^f)$  along with sketches illustrating the relative sizes of the forward and kinking plastic zones for the 3 cases labelled 'A' through 'C' on the map.

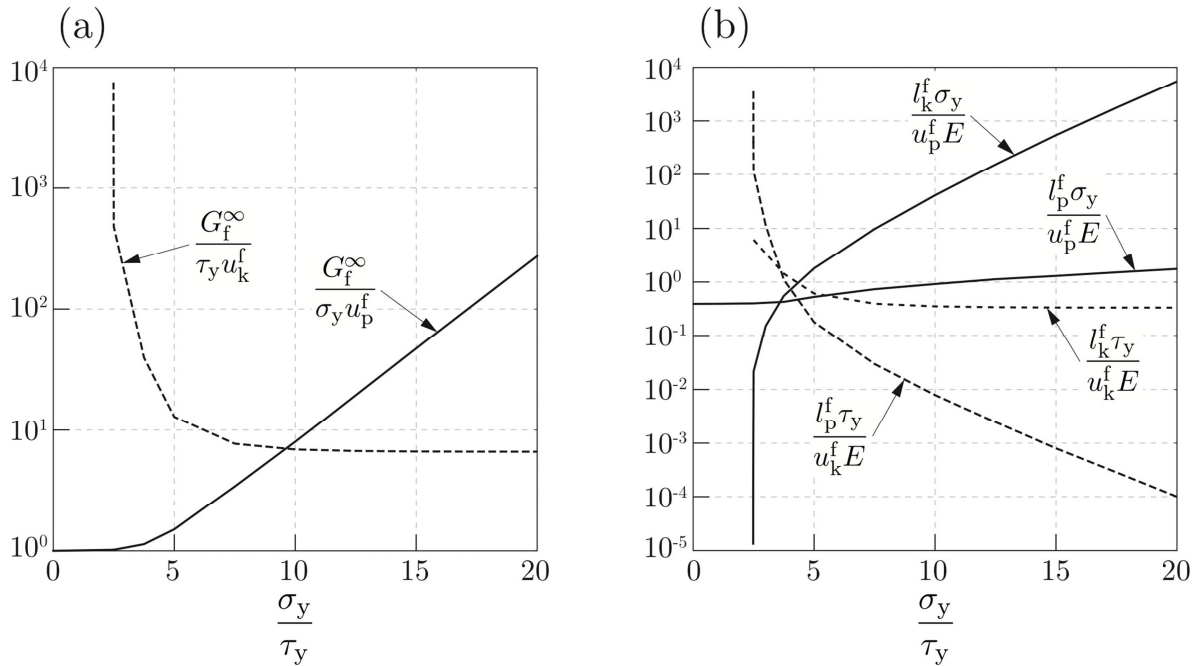


**Fig. 7:** The predicted (a) toughness and (b) lengths of the plastic tensile and shear bands as a function of  $\sigma_y / \tau_y$ . The dashed and solid curves pertain to situations that lie within the kinking and penetration regimes, respectively of the map in Fig. 6.

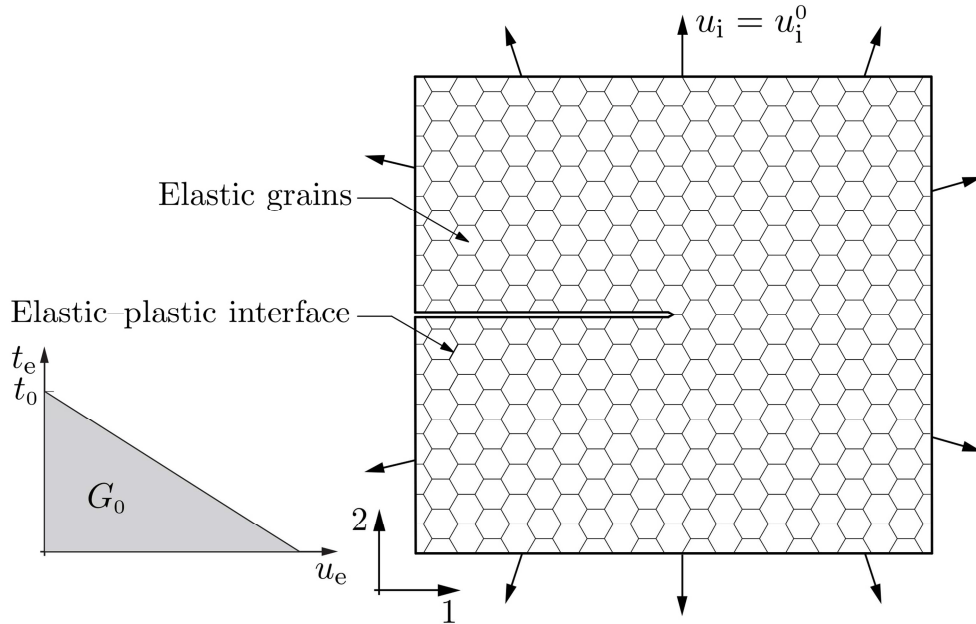


**Fig. 8:** A cracked particulate solid made up of hexagonal elastic grains of dimension  $d$  and glued together by zero thickness elastic-plastic interfaces. The solid is loaded by applying on its boundary the asymptotic mode I  $K$ -field. The effective traction-separation law for the interfaces is depicted in the inset.

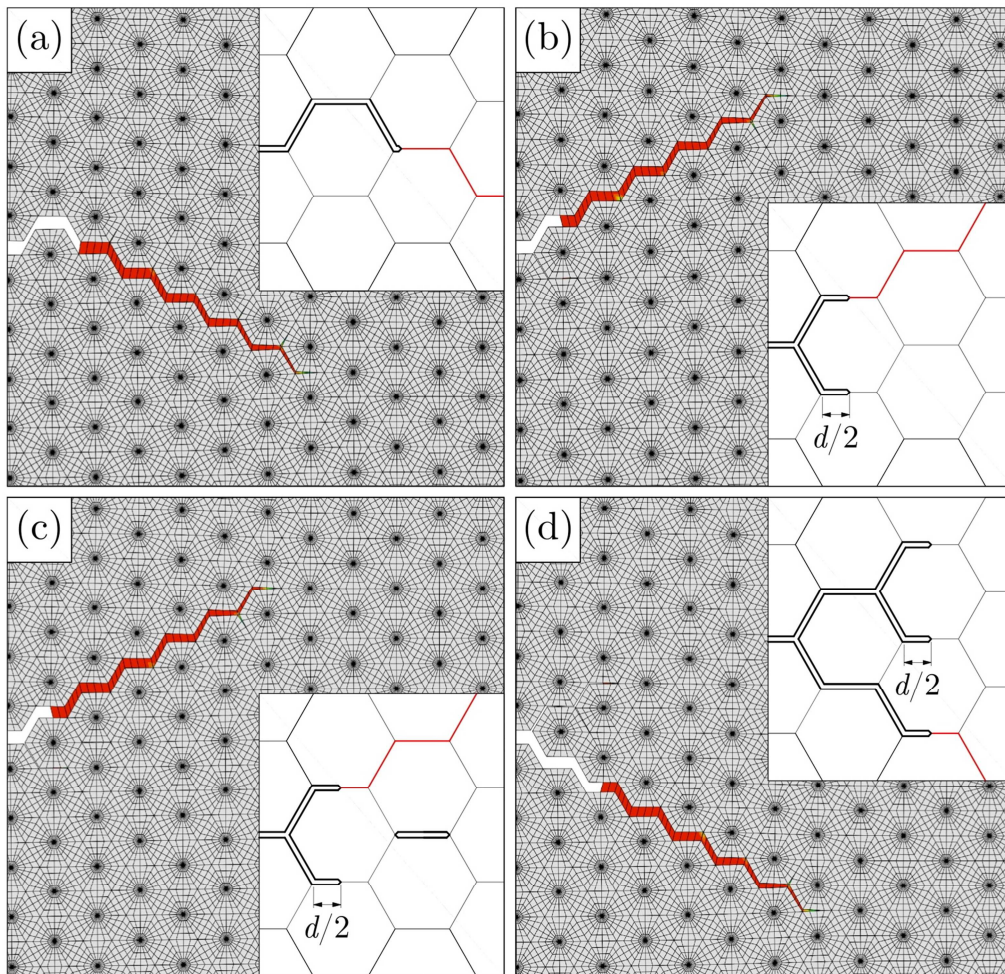


**Fig. 9:** Finite element predictions of the crack paths (shaded in red) for the particulate solid with  $t_0/E = 0.003$ ,  $kd/E = 100$  and  $R_0/d = 1$ . Four initial crack configurations are considered in (a) through (d) as depicted in the insets. The displacement field is magnified by a factor 10 in order to better illustrate the crack paths.

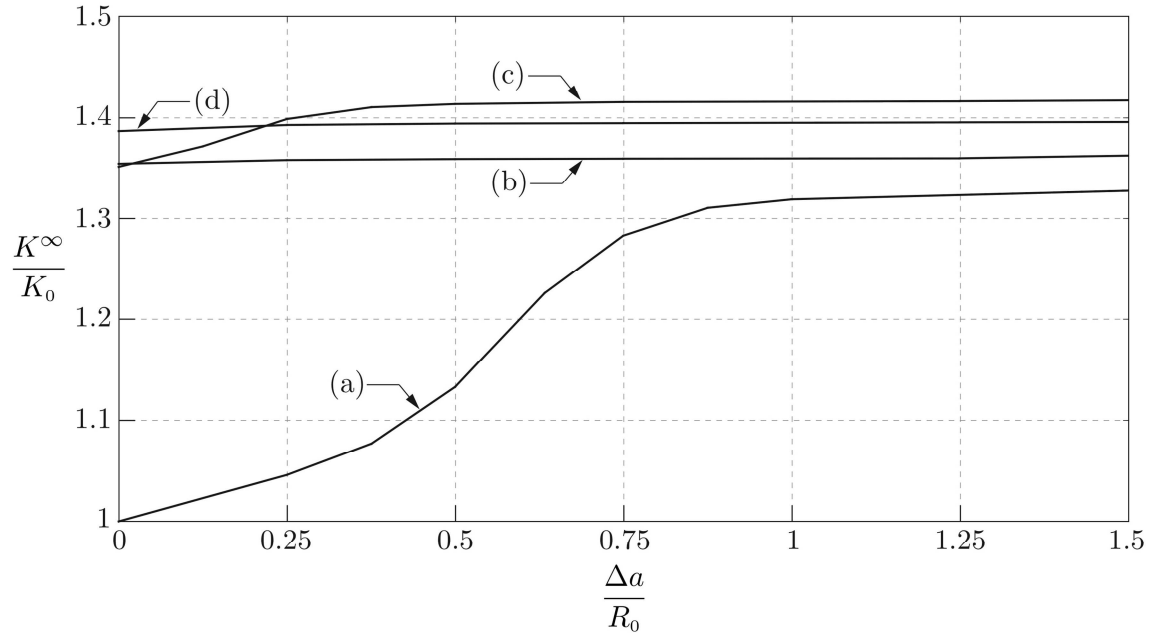


**Fig. 10:** Predictions of the R-curves for the particulate solid with  $t_0/E=0.003$ ,  $kd/E=100$  and  $R_0/d=1$ . Results for four cases corresponding to the initial crack configurations (a) through (d) shown in Fig. 9 are included.

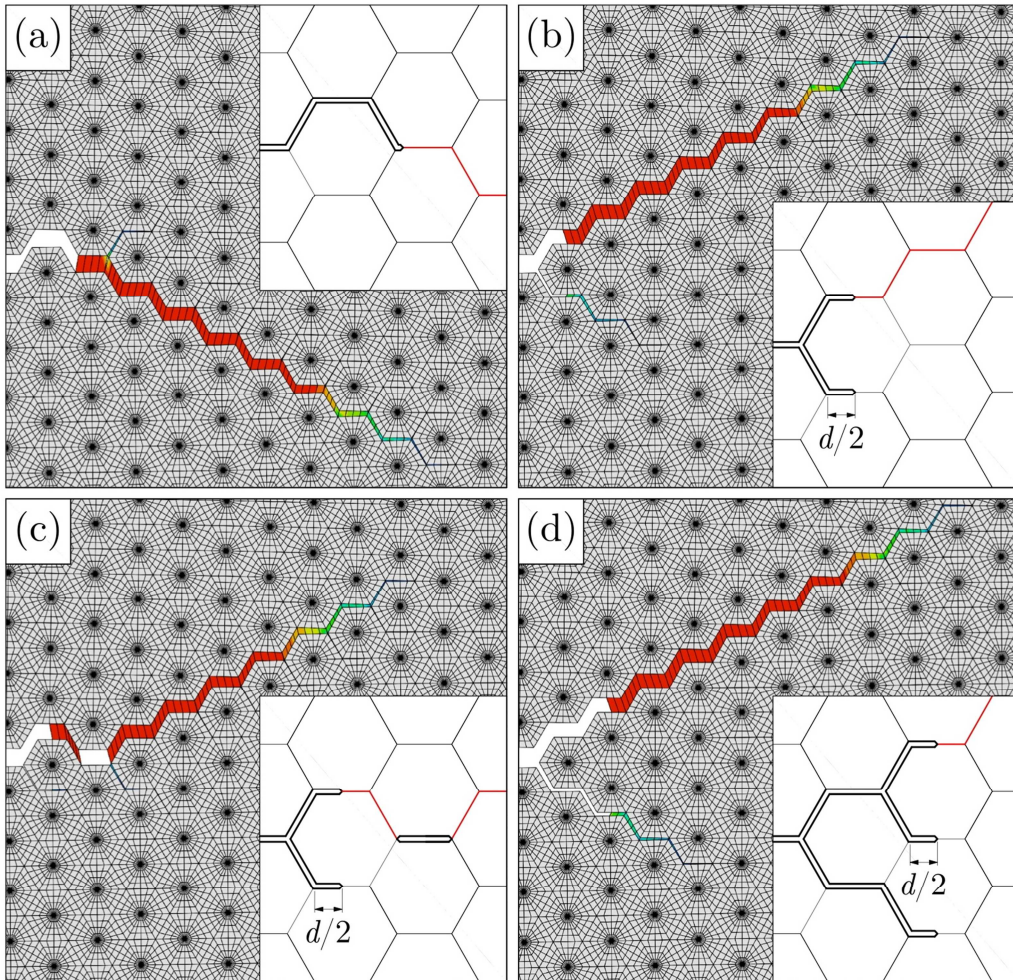


**Fig. 11:** Finite element predictions of the crack paths (shaded in red) for the particulate solid with  $t_0/E=0.003$ ,  $kd/E=100$  and  $R_0/d=7$ . Four initial crack configurations are considered in (a) through (d) as depicted in the insets. The displacement field is magnified by a factor 10 in order to better illustrate the crack paths.

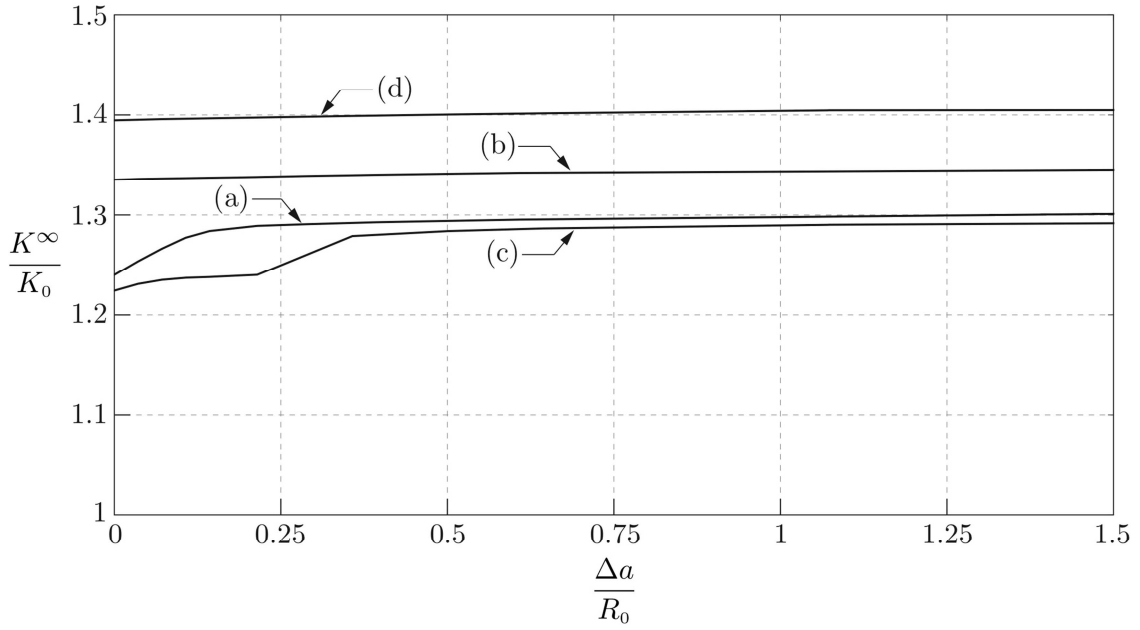


**Fig. 12:** Predictions of the R-curves for the particulate solid with  $t_0/E=0.003$ ,  $kd/E=100$  and  $R_0/d=7$ . Results for four cases corresponding to the initial crack configurations (a) through (d) shown in Fig. 11 are included.

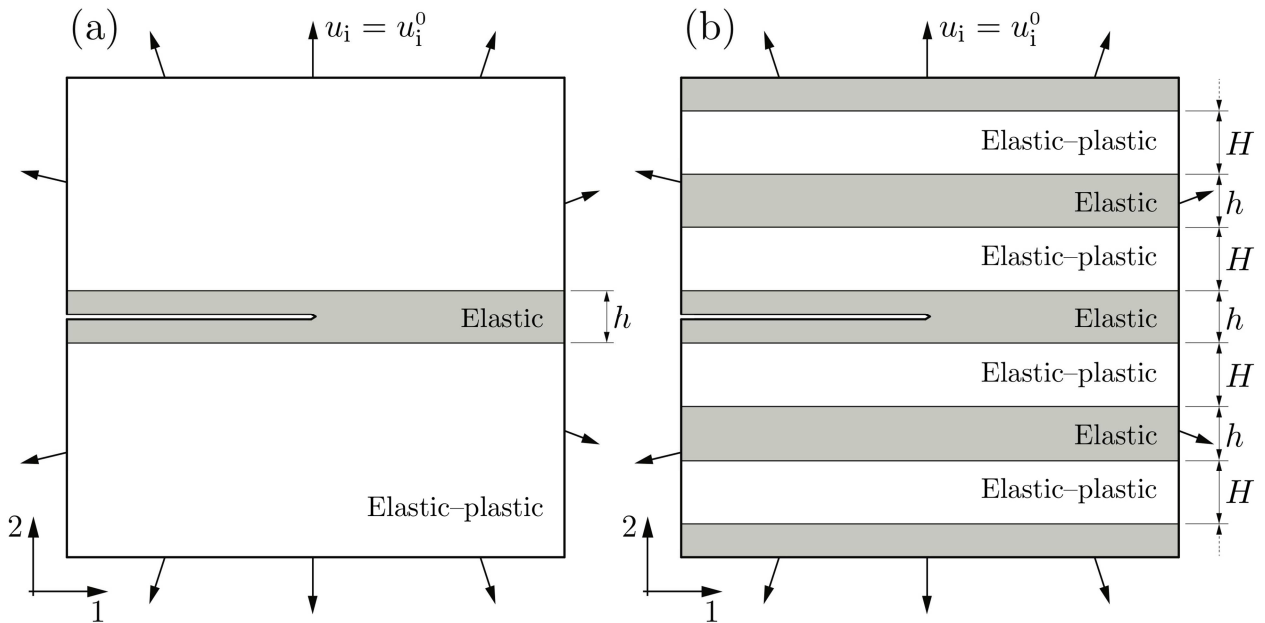


**Fig. 13:** (a) Sketch of the crack in an elastic layer sandwiched between elastic-plastic solids as analyzed by Suo *et al.* (1993) and Tvergaard (1997). (b) Sketch of the cracked multi-layered elastic-plastic composite comprising alternating elastic and elastic-plastic layers of height  $h$  and  $H$ , respectively. The crack lies within an elastic layer as depicted in (b). Both geometries are subjected to a remote mode I  $K$ -field.

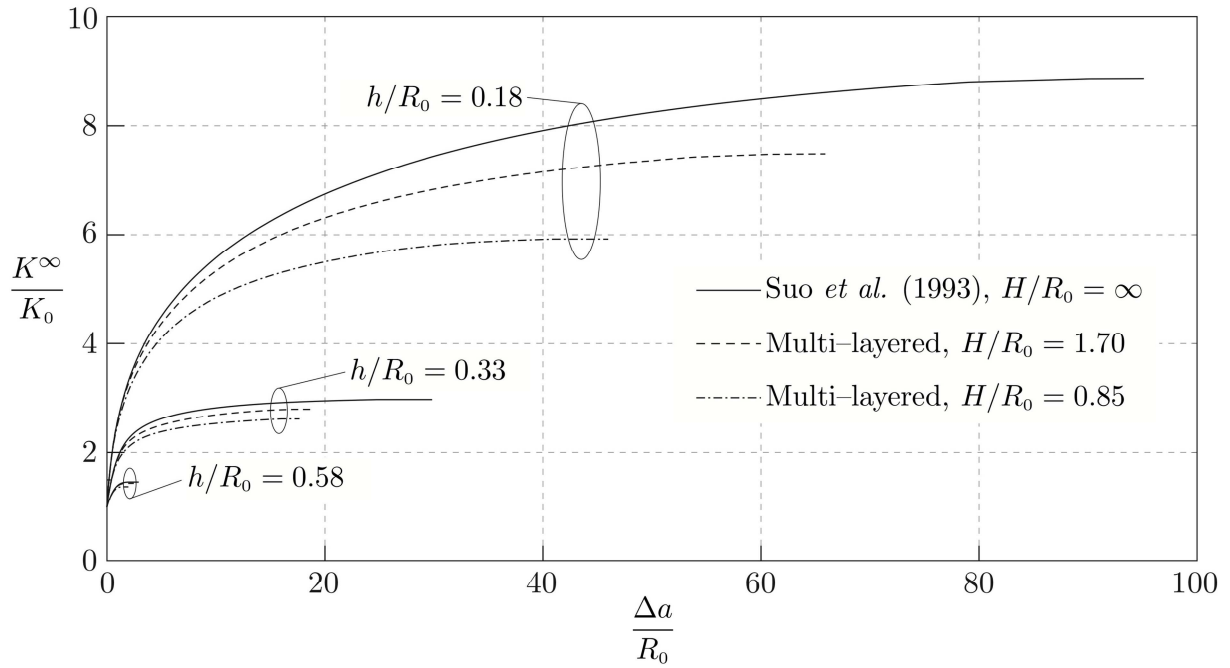


**Fig. 14:** Predictions of the R-curves for the multi-layer composite of Fig.13b for the selected values of  $h/R_0$  and  $H/R_0$ . For each value of  $h/R_0$  we have also included the predicted R-curve for the geometry of Fig. 13a: these results are identical to those presented by Suo *et al.* (1993) and Tvergaard (1997).

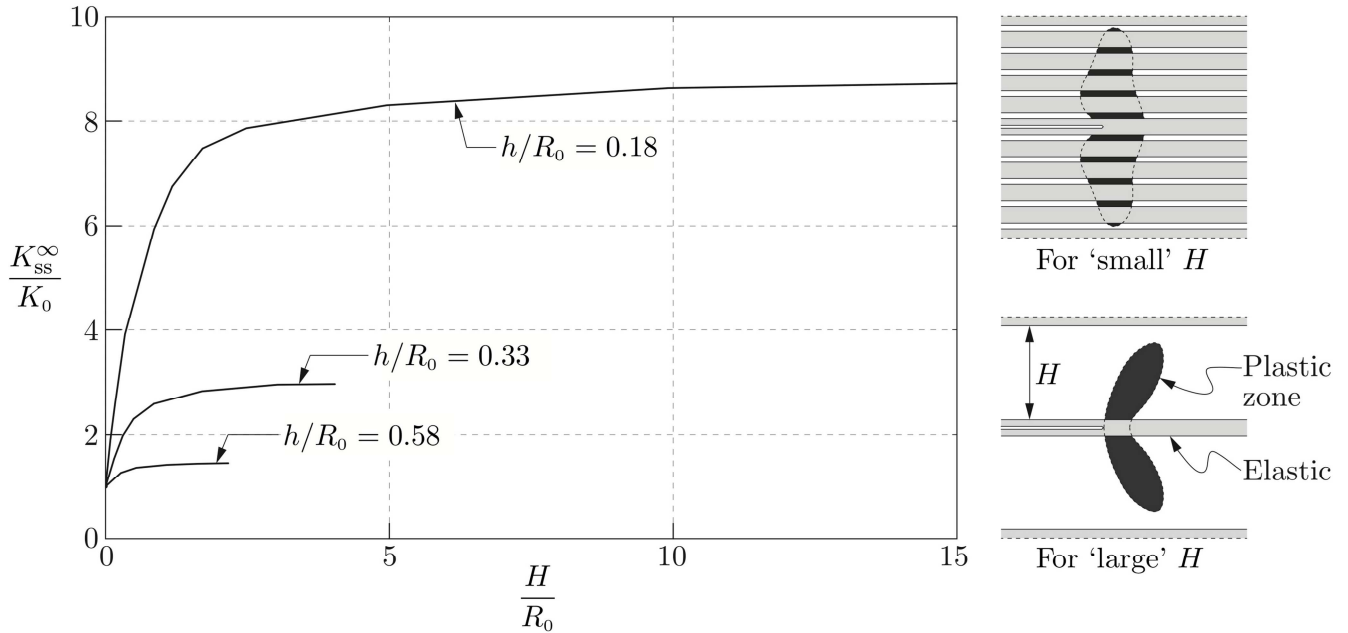


**Fig. 15:** Predictions of the steady-state macroscopic toughness  $K_{ss}^{\infty}/K_0$  in the multi-layered composite of Fig.13b as a function of  $H/R_0$  for selected values of  $h/R_0$ . Sketches depicting the plastic zones for large and small values of  $H$  are included in the inset.